

Bounds on the minimum sound speed above neutron star densities

Dake Zhou^{1,2,3,*}

¹*Department of Physics, University of Washington, Seattle, WA 98195*

²*Institute for Nuclear Theory, University of Washington, Seattle, WA 98195*

³*Department of Physics, University of California Berkeley, Berkeley, CA 94720*

(Dated: August 30, 2024)

We show that the existence of massive neutron stars and asymptotic freedom of QCD place robust upper bounds on the lowest sound speed of the ultra-dense matter unattainable in neutron stars. Our approach does not rely on explicitly representing the equation of state in the density range $\sim 2 - 40n_0$, and does not require probabilistic interpretations. The upper limit decreases rapidly when the maximum mass of neutron stars is greater than about $2.5M_\odot$. Discovery of $\sim 3M_\odot$ neutron stars would strongly support first-order phase transitions at high baryon densities.

I. INTRODUCTION

The nature of quark deconfinement at zero temperature and finite density is an outstanding question in the Standard Model. It remains unclear if the quark and nucleonic phases are separated by phase transitions and efforts to identify a critical point in the QCD phase diagram using heavy-ion experiments remain inconclusive [1, 2]. The liberation of quarks from hadrons can either occur through a smooth crossover [3–5], through a first-order phase transition (FOPT) [6–9], or both hadrons and quarks could coexist over a wide range of densities [10, 11].

Neutron stars (NSs) offer a unique window to address this question since their interior probes a considerable region of cold QCD where the baryon number density may reach $n_B \sim 2 - 10n_0$ ($n_0 = 0.16 \text{ fm}^{-3}$). It is well-known that sufficiently strong FOPT inside NSs can significantly lower maximum mass of NSs and may result in a third family of compact stars with masses similar to NSs but distinct sizes (e.g. [12–14]). Here, we point out that FOPTs *above* NS densities not realized in nature can also be inferred from astrophysical observations. We shall show that the minimum of squared sound speed $C_s = c_s^2$ is bounded from above. Depending on the details of the microscopic interactions, FOPTs manifest as periods of vanishing or low C_s . Evidence for diminished C_s thus would lend support for FOPT in cold QCD. Previous work has shown that the maximum of sound speed squared $C_{s,\text{max}}$ most likely exceeds $1/3$ in order to explain the existence of two-solar-mass pulsars, either model-independently [15, 16] or via statistical inferences [17, 18]. Since C_s asymptotes to $1/3$ from below, indications of $C_{s,\text{max}} > 1/3$ inside NSs necessitate a trough in C_s with $C_{s,\text{min}} < 1/3$ above NS densities, though its numerical value remains undetermined. The present letter aims to fill this gap.

Our main finding is that the NS maximum mass, commonly known as the Tolman–Oppenheimer–Volkoff limit M_{TOV} [19, 20], places robust bounds on $C_{s,\text{min}}$ above

NS densities. Presently, the heaviest known pulsars are around $2M_\odot$ [21–25]. While multimessenger observations of the post-merger evolution of GW170817 [26] likely indicate $M_{\text{TOV}} \lesssim 2.2 - 2.3M_\odot$ [27–31], the possibility of higher M_{TOV} has yet to be conclusively ruled out. In particular, the mass of the secondary component of GW190814 is inferred to be $2.59_{-0.09}^{+0.08}M_\odot$ [32]. Its implication for NS interiors has been explored previously in refs [15, 33, 34] assuming it is an NS, and here we focus on its impacts above NS densities motivated by the fact that future gravitational wave observations could dramatically increase the sample of observed NS masses [35, 36].

Probing the ultra-dense matter not realized in NSs is enabled by taking a global view of the entire zero-temperature QCD phase diagram. This strategy of combining information about the equation of state (EOS) of cold dense matter at low density where nuclear physics provides guidance, intermediate density where NS constraints are useful, and high density where perturbative QCD (pQCD) is applicable [37–44] have been explored in recent work [45–49]. Employing previously-known model-independent bounds on the EOS [15, 50–52], in [49] we clarified that while pQCD may exclude a considerable fraction of EOSs in scenarios where $C_{s,\text{max}} \gtrsim 0.6$ inside NSs, it cannot improve bounds on NS masses and radii. Additionally, we pointed out that the existence of $2M_\odot$ NSs places robust limits on non-perturbative effects at ultra-high densities unattainable in NSs. This work expands model-independent bounds on the ultra-dense matter.

The rest of the manuscript is organized as follows. Sections II and III introduce bounds on the extrema of C_s over an arbitrary interval of baryon chemical potential $\mu_B \in [\mu_L, \mu_H]$. They follow from the requirements that the baryon number density n_B and separately the pressure P at the endpoints L and H are consistent with zero-temperature thermodynamics. For any neutron star model, we apply these bounds between μ_B at the center of most massive NSs which we label μ_{TOV} , and the lowest baryon chemical potential μ_{pQCD} down to which pQCD is believed to remain valid. This leads to upper bounds on $C_{s,\text{min}}$ over $[\mu_{\text{TOV}}, \mu_{\text{pQCD}}]$ specific to each NS EOS.

* dkzhou@berkeley.edu

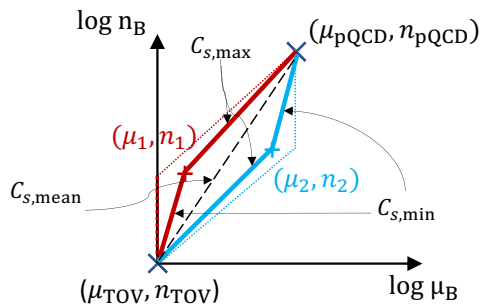


FIG. 1. Schematics for the mean value bound eq. 3 and the ΔP_{\max} bound eq. 10. The maximally stiff and soft EOSs between the low- and high-density endpoints are shown in blue and red respectively. The dotted lines show these limits when $C_{s,\min} = 0$ and $C_{s,\max} = 1$, the solid lines depict generalized bounds with $C_{s,\min} > 0$ and $C_{s,\max} < 1$. The dashed line in black is the secant whose slope is $C_{s,\text{mean}}^{-1}$ eq. 2.

Next, in section IV we remove dependencies on the NS inner core EOS by maximizing the resulting upper bounds among all physical possibilities.

II. THE MEAN VALUE BOUND

We begin by deducing a bound on the extrema of C_s from the properties of the function $n_B(\mu_B)$. At any point in the μ_B - n_B plane, the speed of sound squared C_s of a given EOS is related to the slope via the thermodynamic relation

$$\frac{d \log n_B}{d \log \mu_B} = C_s^{-1}. \quad (1)$$

This bound is based on the dashed black line in fig. 1, the secant connecting low- and high-density endpoints. The inverse of its slope, which we denote $C_{s,\text{mean}}$ (whose meaning will be clear shortly), is given by

$$C_{s,\text{mean}} = \frac{\log(\mu_{\text{pQCD}}/\mu_{\text{TOV}})}{\log(n_{\text{pQCD}}/n_{\text{TOV}})}, \quad (2)$$

where $n_{\text{pQCD}} \equiv n_B(\mu_{\text{pQCD}})$ is prediction by pQCD, and both n_{TOV} and μ_{TOV} are specific to each NS model.

By the mean value theorem, for any EOS that passes through the specified endpoints there exists at least one point inside the interval where the slope is given by that of the secant $C_{s,\text{mean}}^{-1}$. It follows that the minimum and maximum of C_s must bracket $C_{s,\text{mean}}$, i.e.,

$$C_{s,\min} \leq C_{s,\text{mean}} \leq C_{s,\max}. \quad (3)$$

The *mean value bound* eq. 3 does not make use of the pressure information at the endpoints so only provides

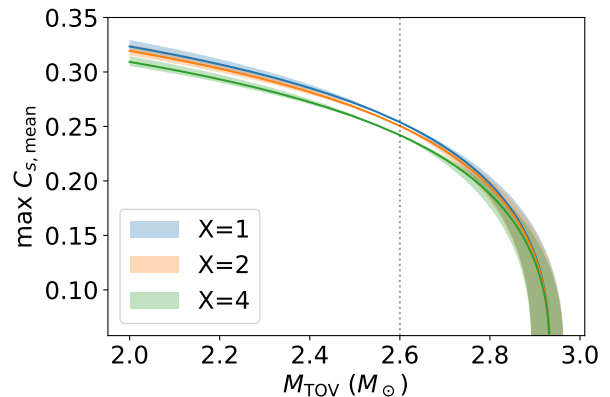


FIG. 2. Upper bounds on the mean value eq. 2 maximized across all NS EOSs (see section IV for details). By the mean value bound eq. 3 they are also upper limits on $C_{s,\min}$. The lines and the bands correspond to the central value and the 2σ uncertainties of chiral effective field theory (χEFT). Each color represents a choice of the pQCD renormalization scale $X = \bar{\Lambda}/(\mu_B/3)$. All physical possibilities lie on or below these bounds, assuming χEFT is valid up to $2n_0$.

a conservative limit. Nevertheless, it is robust against pQCD uncertainties as n_{pQCD} is known within $\sim 10\%$, a consequence of accurate pQCD predictions for C_s^{pQCD} and eq. 1. Properties of the logarithm further ensure $C_{s,\text{mean}}$ is insensitive to the choice of μ_{pQCD} .

Figure 2 shows upper limits on $C_{s,\text{mean}}$ as a function of NS maximum mass M_{TOV} . By eq. 3 they are also upper limits on $C_{s,\min}$. These bounds strengthen rapidly with increasing M_{TOV} , and are insensitive to nuclear theory uncertainties. The details and the procedure to obtain these results will be discussed in section IV.

III. BOUNDS FROM PRESSURE

Stronger limits on $C_{s,\min}$ are possible by demanding the pressure of cold quark matter in the perturbative regime can be reached from P_{TOV} , the central pressure of the most massive NS. Model-independent lower and upper bounds on the pressure have long been known in the literature [15, 16, 50–52]. Above an arbitrary density which we label L , the lowest (highest) and highest (lowest) pressures at any chemical potential (density) are given by the so-called maximally stiff and maximally soft EOSs respectively. They are depicted in blue and red in

¹ The mean value theorem assumes C_s is continuous and differentiable. A proof relaxing these assumptions is given in appendix A

fig. 1 and are specified by

$$C_s(n_B) = \begin{cases} C_{s,\max}, & n_B \leq n_L + \Delta n_{\text{onset}} \\ C_{s,\min}, & n_B > n_L + \Delta n_{\text{onset}} \end{cases} \quad \text{max stiff,} \quad (4)$$

$$C_s(n_B) = \begin{cases} C_{s,\min}, & n_B \leq n_L + \Delta n_{\text{PT}} \\ C_{s,\max}, & n_B > n_L + \Delta n_{\text{PT}} \end{cases} \quad \text{max soft.} \quad (5)$$

The onset density Δn_{onset} in the maximally stiff and the strength Δn_{PT} in the maximally soft constructions associated with $C_{s,\min}$ segments are uniquely determined by M_{TOV} when employed to describe NS inner cores, or by the high-density boundary condition (n_H, P_H, μ_H) when constraining the EOS between endpoints L and H . In this section, eqs. 4 and 5 are used for the latter purpose, and the endpoints are taken to be the TOV and the pQCD points. While previous work [15, 16] focused on $C_{s,\max}$ assuming $C_{s,\min} = 0$, our aim is to infer $C_{s,\min}$.

The increment in pressure from μ_{TOV} to μ_{pQCD} predicted by these limiting EOSs follows directly from the thermodynamic relation $dP/d\mu_B = n_B$, i.e., the areas beneath these EOSs in fig. 1:

$$\Delta P = \int_{\mu_{\text{TOV}}}^{\mu_{\text{pQCD}}} n_B(\mu_B) d\mu_B, \quad (6)$$

where $n_B(\mu_B)$ is obtained by integrating eq. 1. Denote $\alpha = C_{s,\max}^{-1}$ and $\beta = C_{s,\min}^{-1}$, the maximal gain in pressure associated with the maximally soft EOS is given by

$$\Delta P_{\max} = \frac{n_{\text{pQCD}}\mu_{\text{pQCD}}}{\alpha + 1} \left[1 - \left(\frac{\mu_1}{\mu_{\text{pQCD}}} \right)^{\alpha+1} \right] + \frac{n_{\text{TOV}}\mu_{\text{TOV}}}{\beta + 1} \left[\left(\frac{\mu_1}{\mu_{\text{TOV}}} \right)^{\beta+1} - 1 \right]. \quad (7)$$

Above, μ_1 specifies the transition point marked as red “+” in fig. 1 where C_s is switched from $C_{s,\min}$ to $C_{s,\max}$. This transition point is

$$\mu_1 = \mu_{\text{TOV}} \left(\frac{\mu_{\text{TOV}}}{\mu_{\text{pQCD}}} \right)^{\frac{\delta}{1-\delta}} \left(\frac{n_{\text{pQCD}}}{n_{\text{TOV}}} \right)^{\frac{C_{s,\min}}{1-\delta}}, \quad (8)$$

$$n_1 = n_{\text{TOV}} \left(\frac{n_{\text{pQCD}}}{n_{\text{TOV}}} \right)^{\frac{1}{1-\delta}} \left(\frac{\mu_{\text{TOV}}}{\mu_{\text{pQCD}}} \right)^{\frac{\alpha}{1-\delta}}, \quad (9)$$

where $\delta = C_{s,\min}/C_{s,\max} = \alpha/\beta$.

The expressions for n_2 , μ_2 , and ΔP_{\min} associated with the maximally stiff EOS (blue) are related to eqs. 7 to 9 via swapping $\alpha \leftrightarrow \beta$. We explained in [49] that the undetermined size of non-perturbative superconducting gaps precludes interpreting ΔP_{\min} as a constraint, so only give its expression in appendix B.

For a chosen high-density matching point μ_{pQCD} , stable and causal connections between μ_{TOV} and μ_{pQCD} ex-

ist if and only if [49]

$$\Delta P = P_{\text{pQCD}} - P_{\text{TOV}} \leq \Delta P_{\max}(C_{s,\min}, C_{s,\max}, n_{\text{TOV}}, \mu_{\text{TOV}}). \quad (10)$$

When taking $C_{s,\min} = 0$ and $C_{s,\max} = 1$, eq. 10 is a robust constraint on NS EOSs [46, 48, 49]. Its interpretation becomes murky when $C_{s,\min} > 0$ and/or $C_{s,\max} < 1$. In principle, one may either *assume* values for $C_{s,\min}$ and $C_{s,\max}$ and view eq. 10 as a constraint on NS EOSs through P_{TOV} , n_{TOV} , and μ_{TOV} , or bound $C_{s,\min}$ and $C_{s,\max}$ of the ultra-dense phase via eq. 10 *given* astrophysical inputs that inform the TOV point. Since multimessenger astronomy is expected to provide accurate NS measurements in the coming decade [36], we pursue the second avenue here². As foretold by eq. 3, $C_{s,\min}$ is bounded from above, whose upper limit $\max\{C_{s,\min}\}$ saturates the inequality eq. 10 and is implicitly given by

$$P_{\text{pQCD}} - P_{\text{TOV}} = \Delta P_{\max}(\max\{C_{s,\min}\}, C_{s,\max}, n_{\text{TOV}}, \mu_{\text{TOV}}). \quad (11)$$

Equation 11 is transcendental and we discuss the numerical strategy of solving it in appendix B.

IV. EXTREMIZING OVER NS INNER CORES

To construct neutron stars, we adopt the procedure discussed in [49]. Our approach centers on the state-of-art next-to-next-to-next leading order (N3LO) chiral effective field theory (χ EFT) predictions for pure neutron matter [53, 54], and accurately captures both the central values and correlated truncation errors. The beta-equilibrium EOS is then constructed via a fifth-order expansion in proton fraction (for details see [55]). As for the NS inner core above $n_B = 2n_0$, it is suffice for now to assume some form of EOS is adopted.

For an arbitrary NS model that follows our χ EFT-based low-density EOS up to $n_{\chi\text{EFT}}$ and truncated at its TOV point, the mean value $C_{s,\text{mean}}$ eq. 2 gives an upper bound on $C_{s,\min}$ eq. 3 among all possibilities over the range $[\mu_{\text{TOV}}, \mu_{\text{pQCD}}]$. We then extremize $C_{s,\text{mean}}$ across all physical inner core EOSs at given M_{TOV} to obtain the *global* maximum $\max\{C_{s,\text{mean}}\}$ independent of models over the range between $n_{\chi\text{EFT}}$ and μ_{pQCD} . We will report the technical details of the extremization process elsewhere, and present the results here. We find that $\max\{C_{s,\text{mean}}\}$ is reached by the maximally stiff inner core EOS eq. 4 where $n_L = n_{\chi\text{EFT}}$ and Δn_{onset} is uniquely determined by M_{TOV} :

$$C_s(n_B) = \begin{cases} C_{s,\max}, & n_B \leq n_{\chi\text{EFT}} + \Delta n_{\text{onset}} \\ C_{s,\min}, & n_B > n_{\chi\text{EFT}} + \Delta n_{\text{onset}} \end{cases} \quad (12)$$

² If *ab-initio* limits on $C_{s,\min}$ become available, our framework can be readily turned around to constrain NSs.

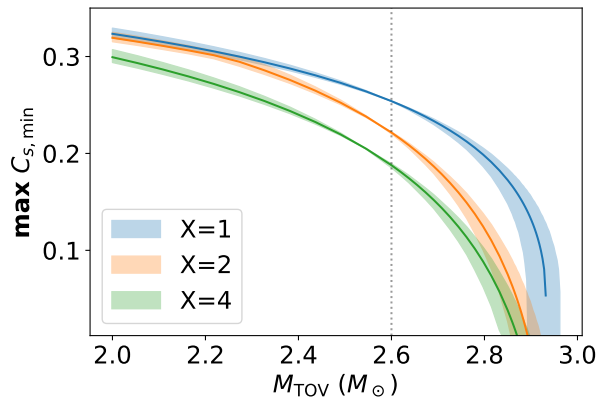


FIG. 3. $\max\{C_{s,\min}\}$, $\max\{C_{s,\min}\}$ from eq. 11 maximized across all NS EOSs. The colors and lines are consistent with those in fig. 2.

If $C_{s,\min}$ in eq. 12 were to vanish identically, the constant $C_{s,\min}$ piece would not be realized in nature, since there is no volume at the center of the most massive NSs for the new phase above FOPT to materialize. However, phase transitions with $C_{s,\min} > 0$ at the center of maximum-mass stars appear to be physical. Although in reality the NS EOS is likely smoother than the maximally stiff inner core, values of $C_{s,\min}$ for any such possibilities would lie below the bounds based on eq. 12, rendering our results conservative. This is confirmed by over a billion NS samples generated from perhaps the most agnostic EOS parameterization, to be reported in the ensuing letter.

The resulting $\max\{C_{s,\text{mean}}\}$ are shown in fig. 2. Throughout the main text we assume χ EFT along with its 2σ uncertainties up to $2n_0$, and impose pQCD at $\mu_{\text{pQCD}} = 2.4 \text{ GeV}$ where the truncation error is estimated by varying the renormalization scale $X \equiv \bar{\Lambda}/(\mu_B/3) = 1, 2, 4$. We employ the N2LO quark matter EOS [37, 38] plus the $\mathcal{O}(\alpha_s^3 \log^2 \alpha_s)$ contribution at N3LO [42, 43], and use two-loop running of α_s . Since χ EFT and pQCD are the sole assumptions, our result only depends on the central values and uncertainties of their predictions. Higher pQCD renormalization scales X yield stronger limits since they predict higher n_{pQCD} and enhance the denominator in eq. 2. Uncertainties associated with χ EFT are generally negligible except near the highest M_{TOV} , where $\sim 40\%$ errors on the pressure $P(n_B = 2n_0)$ translate to $\sim 0.1M_{\odot}$ uncertainties on M_{TOV} . This combined with the steep drop in $\max\{C_{s,\text{mean}}\}$ leads to increased sensitivities toward χ EFT uncertainties when $M_{\text{TOV}} \gtrsim 2.8M_{\odot}$. A detailed account on the uncertainties of these bounds is presented in appendix D.

Following a similar extremization process, the global maximum of $\max\{C_{s,\min}\}$ across all high-density NS models at fixed M_{TOV} can be obtained, and is again given by the maximally stiff inner core EOS. For clarity we use boldfaced $\max\{C_{s,\min}\} \equiv \max_{\text{NS}}\{\max\{C_{s,\min}\}\}$ to dis-

tinguish this limit extremized across EOSs both below and above NS densities from $\max\{C_{s,\min}\}$ that is specific to each NS EOS. The results are shown in fig. 3. Compared to the mean values bounds in fig. 2, the constraints here are stronger since the pressure information is taken into account. But this improvement comes at the expense of amplified uncertainties due to the poorly determined P_{pQCD} . All in all, if a NS was involved in GW190814, $C_{s,\min}$ is robustly placed below $\sim 0.2 - 0.25$, a bound strengthens to $C_{s,\min} \lesssim 0.15$ if $M_{\text{TOV}} \gtrsim 2.9M_{\odot}$.

So far, only causality $C_{s,\text{max}} = 1$ is imposed. Stronger assumptions on $C_{s,\text{max}}$ can lead to tighter constraints on $C_{s,\min}$. This possibility is demonstrated in fig. 4. For instance, the current putative value $M_{\text{TOV}} \simeq 2.2M_{\odot}$ [27–31] places $C_{s,\min}$ below ~ 0.25 if $C_{s,\text{max}} \lesssim 0.5$. On one hand, decreasing $C_{s,\text{max}}$ above NS densities (in eq. 10) reduces ΔP_{max} , the area below the red curve in fig. 1. Ensuring eq. 10 remains satisfied and saturated, i.e., fixing the area ΔP_{max} , thus requires lower $\max\{C_{s,\min}\}$. On the other hand, reducing $C_{s,\text{max}}$ inside NSs at fixed M_{TOV} necessitates an extended $C_{s,\text{max}}$ segment inside NSs, which generally leads to lower $\max\{C_{s,\min}\}$ above NS densities (full explanation given below).

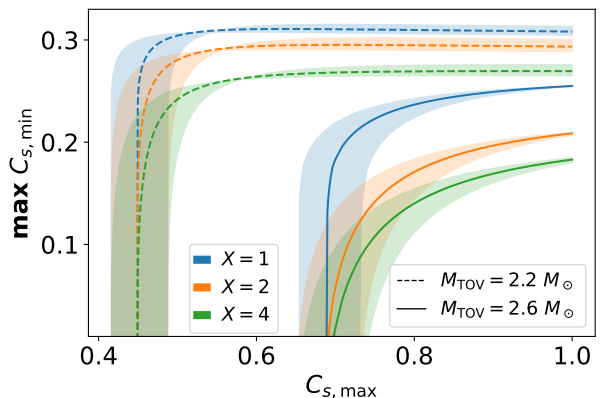


FIG. 4. $\max\{C_{s,\min}\}$ as a function of $C_{s,\text{max}}$. The colors and bands are consistent with those in fig. 2. The dashed lines are for $M_{\text{TOV}} = 2.2M_{\odot}$ and the solid for $M_{\text{TOV}} = 2.6M_{\odot}$.

V. DISCUSSION

The main result of this work can be simply understood by considering the mean values between χ EFT and pQCD densities, $C_{s,\text{mean}}^{\chi\text{EFT,pQCD}}$. They are listed in the last column of table I and are very close to $1/3$. The mean value bounds eq. 3 suggest that the “average” of C_s between $n_{\chi\text{EFT}}$ and n_{pQCD} cannot diverge too much from $C_{s,\text{mean}}^{\chi\text{EFT,pQCD}}$, although sizable local deviations are permitted. Elevated C_s over a wide density ranges required to support a high M_{TOV} thus must be compensated by segments of low C_s above NS densities.

Intriguingly, the mean value bound on $C_{s,\max}$ (second inequality in eq. 3) also suggests that the conformal limit $C_{s,\max} \leq 1/3$ [56, 57] if not breached is maximally saturated in dense QCD, an observation independent of any neutron star physics (see appendix C).

X	P (GeV/fm ³)	n_B (n_0)	C_s	$C_{s,\text{mean}}^{\chi\text{EFT,pQCD}}$
1	1.24	30.5	0.365	$0.308^{+0.014}_{-0.011}$
2	2.68	31.3	0.311	$0.305^{+0.014}_{-0.011}$
4	3.07	33.5	0.319	$0.298^{+0.014}_{-0.011}$

TABLE I. The pQCD EOS at $\mu_B = 2.4$ GeV. The last column shows the mean value between $n_{\chi\text{EFT}} = 2.0n_0$ and $\mu_{\text{pQCD}} = 2.4$ GeV. The uncertainties are due the 2σ error of χEFT , where the upper (lower) range corresponds to the soft (stiff) side. Our χEFT -based EOS becomes unstable below $\sim -1.7\sigma$ and is cut off at this value.

Our bounds carry little information about the location of the minimum, except that it is above μ_{TOV} . The value of μ_{TOV} is highly model-dependent [49], but is bounded from both sides by the maximally soft and maximally stiff NS EOSs. These are shown in fig. 6 in appendix D. Additionally, the strength of phase transitions, i.e., the jump in density $\Delta n_B = n_1 - n_{\text{TOV}}$ (see eq. 9) associated with the constant $C_{s,\min}$ piece is bounded from above (lower $C_{s,\min}$ allows for milder Δn_B). We postulate this upper limit is again given by the maximally stiff NS inner core. Upper bounds on Δn_B can thus be translated to stronger limits on $C_{s,\min}$. For details see appendix D.

A key ingredient underlies our results is the near-conformal pQCD predictions for the massless and gapless quark matter where C_s^{pQCD} remains close to $1/3$ and uncertainties tightly controlled even with naive extrapolations down to non-perturbative regimes. This can be traced back to the absence of $\mathcal{O}(\alpha_s)$ contributions to the trace anomaly [58]. We note that while both the strange quark mass m_s and the superconducting gap Δ_{CFL} would quantitatively (but moderately at best since the quark matter EOS is only considered at $\mu_q \sim \text{GeV} \gg m_s, \Delta_{\text{CFL}}$) affect our bounds [49, 59], none of these neglected effects appear to offer a complete explanation of $C_{s,\min} \lesssim 1/3$ on their own. Since $P_{\text{CFL}} \sim \Delta_{\text{CFL}}^2 \mu_B^2$ where $\Delta_{\text{CFL}} \propto \mu_B g_s^{-5} \exp(-1/g_s)$ from the leading order gap equation [60–66], pairing gaps alone predict $C_s \gtrsim 1/3$. On the other hand, phase transitions from either nucleonic or asymmetric quark phases such as the two-flavor color superconductor [67, 68] could explain $C_s \lesssim 1/3$. Furthermore, at N2LO [40] the strange quark mass does not produce a dip below ~ 0.3 , though higher order corrections may change this. One possible alternative cause of the trough in C_s is hyperon condensation. Distinguishing or disentangling its effect from FOPT likely requires precise determinations of $C_{s,\min}$. Our work thus motivates *ab-initio* calculations of dense hyperon gases.

Besides M_{TOV} , we do not find additional NS static ob-

servables including radii and tidal deformabilities for a wide range of NS masses that may robustly inform $C_{s,\min}$, although weak correlations between $C_{s,\min}$ and the size of NSs may emerge for certain subgroups of NS models. As pointed out in the preceding paper [49], μ_{TOV} and n_{TOV} would largely decouple from observables at lower NS masses for sufficiently flexible EOSs. Along with the shallow slopes $\frac{dM}{dR} \sim 0$ near M_{TOV} this highlights the difficulty of constraining the TOV point from measurements of NS sizes. Caveats associated with interpreting confidence interval-based statistical evidence will be discussed in the ensuing letters.

ACKNOWLEDGMENT

It is a pleasure to thank Sanjay Reddy for discussions and carefully reading a draft of the manuscript. During the conception and completion of this work the author is supported by the Institute for Nuclear Theory Grant No. DE-FG02-00ER41132 from the Department of Energy, and by NSF PFC 2020275 (Network for Neutrinos, Nuclear Astrophysics, and Symmetries (N3AS)).

Appendix A: A proof of the mean value bound eq. 3

The speed of sound squared $C_s(n)$ for thermodynamically stable matter at zero temperature may contain a finite number of discontinuities or non-differentiable singularities, but must be a Lebesgue integrable function, whose integral yields the chemical potential. Therefore, by the fundamental theorem of calculus,

$$\begin{aligned} \log \mu(n_H) - \log \mu(n_L) &= \int_{\log n_L}^{\log n_H} C_s(n) d \log n \\ &\geq \int_{\log n_L}^{\log n_H} \min \{C_s(n)\} d \log n \\ &= (\log n_H - \log n_L) \min \{C_s(n)\}, \end{aligned} \quad (\text{A1})$$

from which the first half of eq. 3 follows:

$$C_{s,\min} \equiv \min \{C_s(n)\} \leq \frac{\log \mu(n_H) - \log \mu(n_L)}{\log n_H - \log n_L} \equiv C_{s,\text{mean}}. \quad (\text{A2})$$

The proof for the second inequality in eq. 3 follows similarly.

Appendix B: Details of $\Delta P_{\min,\max}$

Here we present the derivations and full expressions of ΔP_{\max} and ΔP_{\min} for generic $C_{s,\min} \geq 0$ and $C_{s,\max} \leq 1$. We begin with ΔP_{\max} . The EOSs of the constant $C_{s,\min}$ and $C_{s,\max}$ segments (red in fig. 1) follow from integrating

eq. 1 and are given by

$$n_B(\mu_B) = \begin{cases} n_{\text{TOV}} \left(\frac{\mu_B}{\mu_{\text{TOV}}} \right)^\beta, & \mu_{\text{TOV}} \leq \mu_B \leq \mu_1 \\ n_{\text{pQCD}} \left(\frac{\mu_B}{\mu_{\text{pQCD}}} \right)^\alpha, & \mu_1 \leq \mu_B \leq \mu_{\text{pQCD}} \end{cases} \quad (\text{B1})$$

where as in the main text we have defined $\alpha = 1/C_{s,\text{max}}$, $\beta = 1/C_{s,\text{min}}$, and μ_1 the baryon chemical potential at which the two segments intersect. This point of intersection is marked by the red “+” in fig. 1, and its coordinate is straightforward to solve:

$$\mu_1 = \mu_{\text{TOV}} \left(\frac{\mu_{\text{TOV}}}{\mu_{\text{pQCD}}} \right)^{\frac{\delta}{1-\delta}} \left(\frac{n_{\text{pQCD}}}{n_{\text{TOV}}} \right)^{\frac{1}{\beta-\alpha}}, \quad (\text{B2})$$

$$n_1 = n_{\text{TOV}} \left(\frac{n_{\text{pQCD}}}{n_{\text{TOV}}} \right)^{\frac{1}{1-\delta}} \left(\frac{\mu_{\text{TOV}}}{\mu_{\text{pQCD}}} \right)^{\frac{\alpha}{1-\delta}}. \quad (\text{B3})$$

Utilizing eq. 6, we arrive at

$$\Delta P_{\text{max}} = \int_{\mu_{\text{TOV}}}^{\mu_1} d\mu n_{\text{TOV}} \left(\frac{\mu}{\mu_{\text{TOV}}} \right)^\beta + \int_{\mu_1}^{\mu_{\text{pQCD}}} d\mu n_{\text{pQCD}} \left(\frac{\mu}{\mu_{\text{pQCD}}} \right)^\alpha, \quad (\text{B4})$$

which evaluates to eq. 7. This is the largest increment in pressure from μ_{TOV} to μ_{pQCD} .

For ΔP_{min} associated with the maximally stiff EOS (blue in fig. 1), since it only differs from ΔP_{max} in the order of the $C_{s,\text{min}}$ and $C_{s,\text{max}}$ segments, the related expressions are obtained by swapping $\alpha \leftrightarrow \beta$ in those of

ΔP_{max} . To begin with, the stiff EOS takes the form

$$n_B(\mu_B) = \begin{cases} n_{\text{TOV}} \left(\frac{\mu_B}{\mu_{\text{TOV}}} \right)^\alpha, & \mu_{\text{TOV}} \leq \mu_B \leq \mu_2 \\ n_{\text{pQCD}} \left(\frac{\mu_B}{\mu_{\text{pQCD}}} \right)^\beta, & \mu_2 \leq \mu_B \leq \mu_{\text{pQCD}} \end{cases} \quad (\text{B5})$$

where the transition point (μ_2, n_2) is given by

$$\mu_2 = \mu_{\text{pQCD}} \left(\frac{\mu_{\text{pQCD}}}{\mu_{\text{TOV}}} \right)^{\frac{\delta}{1-\delta}} \left(\frac{n_{\text{TOV}}}{n_{\text{pQCD}}} \right)^{\frac{1}{\beta-\alpha}}, \quad (\text{B6})$$

$$n_2 = n_{\text{pQCD}} \left(\frac{n_{\text{TOV}}}{n_{\text{pQCD}}} \right)^{\frac{1}{1-\delta}} \left(\frac{\mu_{\text{pQCD}}}{\mu_{\text{TOV}}} \right)^{\frac{\alpha}{1-\delta}}, \quad (\text{B7})$$

and is marked by the blue “+” in fig. 1. It follows that

$$\begin{aligned} \Delta P_{\text{min}} &= \int_{\mu_{\text{TOV}}}^{\mu_2} d\mu n_{\text{TOV}} \left(\frac{\mu}{\mu_{\text{TOV}}} \right)^\alpha \\ &\quad + \int_{\mu_2}^{\mu_{\text{pQCD}}} d\mu n_{\text{pQCD}} \left(\frac{\mu}{\mu_{\text{pQCD}}} \right)^\beta \\ &= \frac{n_{\text{TOV}} \mu_{\text{TOV}}}{\alpha + 1} \left[\left(\frac{\mu_2}{\mu_{\text{TOV}}} \right)^{\alpha+1} - 1 \right] \\ &\quad + \frac{n_{\text{pQCD}} \mu_{\text{pQCD}}}{\beta + 1} \left[1 - \left(\frac{\mu_2}{\mu_{\text{pQCD}}} \right)^{\beta+1} \right]. \end{aligned} \quad (\text{B8})$$

By plugging in the expressions of μ_1 and μ_2 , ΔP_{min} and ΔP_{max} simplify to

$$\Delta P_{\text{max}} = \frac{n_{\text{pQCD}} \mu_{\text{pQCD}}}{\alpha + 1} \left[1 - \left(\frac{\mu_{\text{TOV}}}{\mu_{\text{pQCD}}} \right)^{\frac{1+\alpha}{1-\delta}} \left(\frac{n_{\text{pQCD}}}{n_{\text{TOV}}} \right)^{\frac{1+\alpha}{\beta-\alpha}} \right] + \frac{n_{\text{pQCD}} \mu_{\text{pQCD}}}{\beta + 1} \left[\left(\frac{\mu_{\text{TOV}}}{\mu_{\text{pQCD}}} \right)^{\frac{1+\alpha}{1-\delta}} \left(\frac{n_{\text{pQCD}}}{n_{\text{TOV}}} \right)^{\frac{1+\alpha}{\beta-\alpha}} - \frac{n_{\text{TOV}} \mu_{\text{TOV}}}{n_{\text{pQCD}} \mu_{\text{pQCD}}} \right], \quad (\text{B9})$$

$$\Delta P_{\text{min}} = \frac{n_{\text{TOV}} \mu_{\text{TOV}}}{\alpha + 1} \left[\left(\frac{\mu_{\text{pQCD}}}{\mu_{\text{TOV}}} \right)^{\frac{1+\alpha}{1-\delta}} \left(\frac{n_{\text{TOV}}}{n_{\text{pQCD}}} \right)^{\frac{1+\alpha}{\beta-\alpha}} - 1 \right] + \frac{n_{\text{TOV}} \mu_{\text{TOV}}}{\beta + 1} \left[\frac{n_{\text{pQCD}} \mu_{\text{pQCD}}}{n_{\text{TOV}} \mu_{\text{TOV}}} - \left(\frac{\mu_{\text{pQCD}}}{\mu_{\text{TOV}}} \right)^{\frac{1+\alpha}{1-\delta}} \left(\frac{n_{\text{TOV}}}{n_{\text{pQCD}}} \right)^{\frac{1+\alpha}{\beta-\alpha}} \right]. \quad (\text{B10})$$

Now we discuss the procedure to find $\max\{C_{s,\text{min}}\}$, the highest $C_{s,\text{min}}$ that satisfies the inequality eq. 10, or equivalently the minimum of $\beta = 1/C_{s,\text{min}}$. It saturates the ΔP_{max} bound eq. 10 and is implicitly given by

$$Z = \frac{1}{1+\alpha} [1 - A] + \frac{1}{1+\beta} \left[A - \frac{x}{y} \right], \quad (\text{B11})$$

where for notational simplicity we have defined dimensionless quantities $x = \frac{\mu_L}{\mu_H}$, $y = \frac{n_H}{n_L}$, $A = x^{\frac{1+\alpha}{1-\delta}} y^{\frac{1+\alpha}{\beta-\alpha}}$, and $Z = \frac{P_H - P_L}{\mu_H n_H}$. This is a transcendental equation in either α or β and to the best of the author’s knowl-

edge no analytical solution exists. We therefore solve $\min\{\beta\} \equiv \max\{C_{s,\text{min}}\}$ numerically.

Useful insights may be gleaned from the geometric interpretation of eq. 6, namely ΔP_{max} as the area under the red curve in fig. 1. It ensures $\Delta P_{\text{max}}(C_{s,\text{min}})$ is a smooth and monotonically decreasing function, i.e., shallower slopes of $C_{s,\text{min}}^{-1}$ reduce the area ΔP_{max} below the maximally soft EOS. Therefore, the root $\max\{C_{s,\text{min}}\}$ if exists must be unique on and bracketed by the interval $[0, C_{s,\text{max}}]$. Further, the mean value bound eq. 3 tightens the bracketing interval to $[0, C_{s,\text{mean}}]$. A simple bisection algorithm or methods of similar flavors are thus handy.

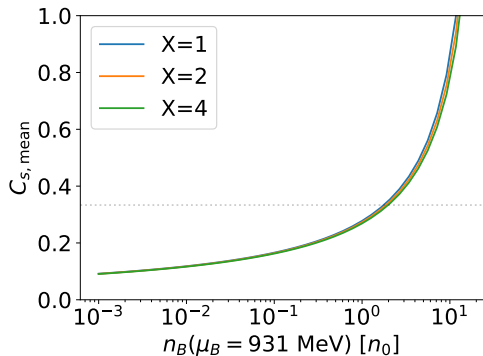


FIG. 5. The mean value between $\mu_{\text{pQCD}} = 2.6$ GeV and the QCD critical point where $\mu_B \approx 931$ MeV. If the ground state near the critical point is strange quark matter, causality demands $n_B(\mu_B = 931 \text{ MeV}) \lesssim 10n_0$, and the conformal limit if hold would require $n_B(\mu_B = 931 \text{ MeV}) \lesssim n_0$.

We note that a solution to eq. B11 is not guaranteed, in which cases even $C_{s,\text{min}} = 0$ that yields the highest possible ΔP_{max} cannot satisfy eq. 10. The NS EOS under consideration is therefore robustly excluded for the specified maximum sound speed $C_{s,\text{max}}$ and pQCD EOS at the chosen μ_{pQCD} [46, 48, 49].

Appendix C: the mean value bound and the conformal limit

In table I we showed that the mean value bound eq. 3 leads to intriguing clues about possible violations of the conformal limit $C_s \lesssim 1/3$, simply by knowing χEFT up to $\sim 2n_0$ and pQCD EOS down to $30 - 50n_0$. This assumes the ground state of low-density QCD is nucleonic and is faithfully described by χEFT . If instead the strange quark matter is favored, eq. 3 may provide useful information on the baryon number density around the critical point $\mu_B \simeq 931$ MeV. The mean value bound suggests $n_B(\mu_B = 931 \text{ MeV}) \lesssim 2n_0$ if the conformal limit were to be respected across all densities in cold QCD, and demand $n_B(\mu_B = 931 \text{ MeV}) \lesssim 10n_0$ on the basis of causality. See fig. 5. These values are insensitive to details of the pQCD EOS (e.g., whether m_s , Δ_{CFL} , or the N3LO contribution are included, or the choices of μ_{pQCD} and X).

Appendix D: the location and strength of $C_{s,\text{min}}$

To begin with, we present bounds on μ_{TOV} and n_{TOV} . Figure 6 shows the lower and upper limits on μ_{TOV} as functions of M_{TOV} . They are given by the maximally stiff and maximally soft inner core EOSs respectively. We also superimpose about 100 million samples of NS EOS on top of it to corroborate these bounds. Our main results

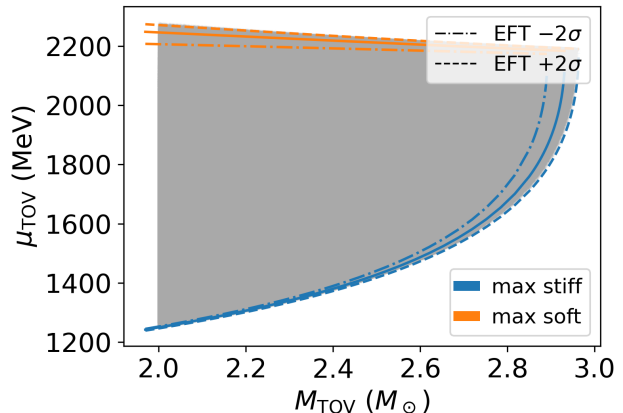


FIG. 6. Lower and upper bounds on μ_{TOV} given by the maximally stiff (blue) and maximally soft (orange) inner core EOSs. $C_{s,\text{min}}$ under scrutiny in this work lies above μ_{TOV} (and below μ_{pQCD}). The gray region consists of $\sim 10^8$ EOS samples, confirming the lower and upper limits.

figs. 2 and 3 are based on the maximally stiff construction (blue). The rapid increase in μ_{TOV} for $M_{\text{TOV}} \gtrsim 2.5M_{\odot}$ is a key reason behind the steep drop in $\max\{C_{s,\text{mean}}\}$ and $\max\{C_{s,\text{min}}\}$ in figs. 2 and 3. An upper bound is also feasible and is given by the maximally soft EOS (orange). It stays around 2.1 – 2.2 GeV for the range of M_{TOV} shown here and always lies above the blue curves.

Predictions for n_{TOV} by eq. 12 are shown as the blue curves in fig. 7. They are not bounds on n_{TOV} , although lower limits can be obtained by setting $C_{s,\text{min}} = 0$ in eq. 12 and are shown in gray. When FOPTs are present at the center of most massive NSs, n_{TOV} are always pushed higher and the magnitude of this change is insensitive to the numerical value of $C_{s,\text{min}}$ as long as $C_{s,\text{min}} \lesssim 0.01$. The only exception is at the highest possible values of M_{TOV} , where adding the $C_{s,\text{min}}$ segment at the center of the star no longer produces stable configurations and the blue and gray curves touch (not shown due to limited resolutions). For a sample-based statistics, see the preceding paper [49].

These information allows one to gain deeper insights into our bounds in figs. 2 and 3. Since eq. 12 (with $C_{s,\text{min}} > 0$) predicts the lowest μ_{TOV} for given M_{TOV} , and at these μ_{TOV} the highest n_{TOV} , it is evident from eq. 2 that it produces the global maxima of $C_{s,\text{mean}}$. Therefore, even if the phase transition in the maximally stiff inner core eq. 12 is shown to be unphysical, all realistic NS EOSs would still have $C_{s,\text{min}}$ below $\max\{C_{s,\text{mean}}\}$ and $\max\{C_{s,\text{min}}\}$ derived from eq. 12. For instance, discounting the $C_{s,\text{min}}$ piece in eq. 12 as unrealistic and setting n_{TOV} to the onset of FOPTs (gray in fig. 7) would reduce the denominator in eq. 2 while leaving the numerator unaffected, decreasing $C_{s,\text{mean}}$. In fact, there exists smooth deformations to eq. 12 (for instance, lowering Δn_{onset} and raising $C_{s,\text{min}}$) in which infinitesimal

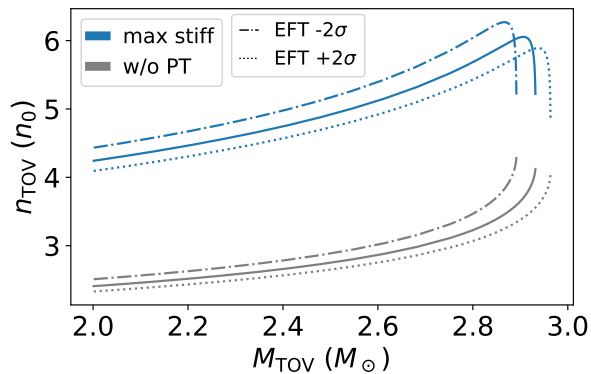


FIG. 7. Predictions of n_{TOV} by the maximally stiff inner core EOS eq. 12 with $C_{s,\text{min}} = 0$ (gray) and $C_{s,\text{min}} = 10^{-6}$ (blue). At given M_{TOV} , lower bounds on n_{TOV} for *any* NS EOS are given by the grey curve (i.e., eq. 12 truncated at the onset of FOPT).

changes to the EOS result in correspondingly small shifts in $C_{s,\text{mean}}$ and $\max\{C_{s,\text{min}}\}$. One can show (at least some of) these neighbors are physical, so eq. 12 remains relevant even if itself may be unrealistic.

The uncertainties in fig. 2 can also be understood better with the help of figs. 6 and 7. At $M_{\text{TOV}} \simeq 2M_{\odot}$, the error in $C_{s,\text{mean}}$ is dominated by that of n_{TOV} where softer χEFT EOSs predict higher central densities and consequently higher $C_{s,\text{mean}}$. Near high values of $M_{\text{TOV}} \gtrsim 2.6M_{\odot}$ the uncertainty in $C_{s,\text{mean}}$ is dominated by that of μ_{TOV} and now softer χEFT EOSs predict higher μ_{TOV} therefore lower values of $C_{s,\text{mean}}$. It is more challenging to pinpoint exactly the sources of errors in fig. 3 due to the rather obscured dependencies on μ_{TOV} and n_{TOV} in $\max\{C_{s,\text{min}}\}$. But since the ΔP_{max} bound is an additional requirement on top of eq. 3 and the bounds in fig. 3 closely tracks those in fig. 2, the uncertainties follow similar trends too.

-
- [1] X. An *et al.*, The BEST framework for the search for the QCD critical point and the chiral magnetic effect, Nucl. Phys. A **1017**, 122343 (2022), arXiv:2108.13867 [nucl-th].
- [2] A. Sorensen *et al.*, Dense nuclear matter equation of state from heavy-ion collisions, Prog. Part. Nucl. Phys. **134**, 104080 (2024), arXiv:2301.13253 [nucl-th].
- [3] T. Schäfer and F. Wilczek, Continuity of quark and hadron matter, Phys. Rev. Lett. **82**, 3956 (1999), arXiv:hep-ph/9811473.
- [4] T. Schäfer and F. Wilczek, Quark description of hadronic phases, Phys. Rev. D **60**, 074014 (1999), arXiv:hep-ph/9903503.
- [5] T. Schäfer, Patterns of symmetry breaking in QCD at high baryon density, Nucl. Phys. B **575**, 269 (2000), arXiv:hep-ph/9909574.
- [6] A. Cherman, S. Sen, and L. G. Yaffe, Anyonic particle-vortex statistics and the nature of dense quark matter, Phys. Rev. D **100**, 034015 (2019), arXiv:1808.04827 [hep-th].
- [7] Y. Hirono and Y. Tanizaki, Quark-Hadron Continuity beyond the Ginzburg-Landau Paradigm, Phys. Rev. Lett. **122**, 212001 (2019), arXiv:1811.10608 [hep-th].
- [8] A. Cherman, T. Jacobson, S. Sen, and L. G. Yaffe, Higgs-confinement phase transitions with fundamental representation matter, Phys. Rev. D **102**, 105021 (2020), arXiv:2007.08539 [hep-th].
- [9] T. T. Dumitrescu and P.-S. Hsin, Higgs-Confinement Transitions in QCD from Symmetry Protected Topological Phases, (2023), arXiv:2312.16898 [hep-th].
- [10] L. McLerran and R. D. Pisarski, Phases of cold, dense quarks at large $N(c)$, Nucl. Phys. A **796**, 83 (2007), arXiv:0706.2191 [hep-ph].
- [11] L. McLerran and S. Reddy, Quarkyonic Matter and Neutron Stars, Phys. Rev. Lett. **122**, 122701 (2019), arXiv:1811.12503 [nucl-th].
- [12] U. H. Gerlach, Equation of State at Supranuclear Densities and the Existence of a Third Family of Superdense Stars, Phys. Rev. **172**, 1325 (1968).
- [13] B. Kampfer, On the Possibility of Stable Quark and Pion Condensed Stars, J. Phys. A **14**, L471 (1981).
- [14] N. K. Glendenning and C. Kettner, Nonidentical neutron star twins, Astron. Astrophys. **353**, L9 (2000), arXiv:astro-ph/9807155.
- [15] C. Drischler, S. Han, J. M. Lattimer, M. Prakash, S. Reddy, and T. Zhao, Limiting masses and radii of neutron stars and their implications, Phys. Rev. C **103**, 045808 (2021), arXiv:2009.06441 [nucl-th].
- [16] C. Drischler, S. Han, and S. Reddy, Large and massive neutron stars: Implications for the sound speed within QCD of dense matter, Phys. Rev. C **105**, 035808 (2022), arXiv:2110.14896 [nucl-th].
- [17] P. Bedaque and A. W. Steiner, Sound velocity bound and neutron stars, Phys. Rev. Lett. **114**, 031103 (2015), arXiv:1408.5116 [nucl-th].
- [18] I. Tews, J. Carlson, S. Gandolfi, and S. Reddy, Constraining the speed of sound inside neutron stars with chiral effective field theory interactions and observations, (2018), arXiv:1801.01923 [nucl-th].
- [19] R. C. Tolman, Static solutions of Einstein's field equations for spheres of fluid, Phys. Rev. **55**, 364 (1939).
- [20] J. R. Oppenheimer and G. M. Volkoff, On Massive neutron cores, Phys. Rev. **55**, 374 (1939).
- [21] P. Demorest, T. Pennucci, S. Ransom, M. Roberts, and J. Hessels, Shapiro Delay Measurement of A Two Solar Mass Neutron Star, Nature **467**, 1081 (2010), arXiv:1010.5788 [astro-ph.HE].
- [22] J. Antoniadis *et al.*, A Massive Pulsar in a Compact Relativistic Binary, Science **340**, 6131 (2013), arXiv:1304.6875 [astro-ph.HE].
- [23] H. T. Cromartie *et al.* (NANOGrav), Relativistic Shapiro delay measurements of an extremely massive millisecond pulsar, Nature Astron. **4**, 72 (2019), arXiv:1904.06759 [astro-ph.HE].
- [24] R. W. Romani, D. Kandel, A. V. Filippenko, T. G. Brink, and W. Zheng, PSR J1810+1744: Companion Darkening and a Precise High Neutron Star Mass, Astrophys. J.

- Lett. **908**, L46 (2021), arXiv:2101.09822 [astro-ph.HE].
- [25] E. Fonseca *et al.*, Refined Mass and Geometric Measurements of the High-mass PSR J0740+6620, *Astrophys. J. Lett.* **915**, L12 (2021), arXiv:2104.00880 [astro-ph.HE].
- [26] B. P. Abbott *et al.* (LIGO Scientific, Virgo), GW170817: Observation of Gravitational Waves from a Binary Neutron Star Inspiral, *Phys. Rev. Lett.* **119**, 161101 (2017), arXiv:1710.05832 [gr-qc].
- [27] B. Margalit and B. D. Metzger, Constraining the Maximum Mass of Neutron Stars From Multi-Messenger Observations of GW170817, *Astrophys. J.* **850**, L19 (2017), arXiv:1710.05938 [astro-ph.HE].
- [28] M. Shibata, S. Fujibayashi, K. Hotokezaka, K. Kiuchi, K. Kyutoku, Y. Sekiguchi, and M. Tanaka, Modeling GW170817 based on numerical relativity and its implications, *Phys. Rev. D* **96**, 123012 (2017), arXiv:1710.07579 [astro-ph.HE].
- [29] L. Rezzolla, E. R. Most, and L. R. Weih, Using gravitational-wave observations and quasi-universal relations to constrain the maximum mass of neutron stars, *Astrophys. J.* **852**, L25 (2018), arXiv:1711.00314 [astro-ph.HE].
- [30] D. Radice, A. Perego, S. Bernuzzi, and B. Zhang, Long-lived Remnants from Binary Neutron Star Mergers, *Mon. Not. Roy. Astron. Soc.* **481**, 3670 (2018), arXiv:1803.10865 [astro-ph.HE].
- [31] M. Shibata, E. Zhou, K. Kiuchi, and S. Fujibayashi, Constraint on the maximum mass of neutron stars using GW170817 event, *Phys. Rev. D* **100**, 023015 (2019), arXiv:1905.03656 [astro-ph.HE].
- [32] R. Abbott *et al.* (LIGO Scientific, Virgo), GW190814: Gravitational Waves from the Coalescence of a 23 Solar Mass Black Hole with a 2.6 Solar Mass Compact Object, *Astrophys. J. Lett.* **896**, L44 (2020), arXiv:2006.12611 [astro-ph.HE].
- [33] D. A. Godzieba, D. Radice, and S. Bernuzzi, On the maximum mass of neutron stars and GW190814, *Astrophys. J.* **908**, 122 (2021), arXiv:2007.10999 [astro-ph.HE].
- [34] F. J. Fattoyev, C. J. Horowitz, J. Piekarewicz, and B. Reed, GW190814: Impact of a 2.6 solar mass neutron star on the nucleonic equations of state, *Phys. Rev. C* **102**, 065805 (2020), arXiv:2007.03799 [nucl-th].
- [35] B. P. Abbott *et al.* (KAGRA, LIGO Scientific, Virgo), Prospects for observing and localizing gravitational-wave transients with Advanced LIGO, Advanced Virgo and KAGRA, *Living Rev. Rel.* **19**, 1 (2016), arXiv:1304.0670 [gr-qc].
- [36] V. Kalogera *et al.*, The Next Generation Global Gravitational Wave Observatory: The Science Book, (2021), arXiv:2111.06990 [gr-qc].
- [37] B. A. Freedman and L. D. McLerran, Fermions and Gauge Vector Mesons at Finite Temperature and Density. 1. Formal Techniques, *Phys. Rev. D* **16**, 1130 (1977).
- [38] B. A. Freedman and L. D. McLerran, Fermions and Gauge Vector Mesons at Finite Temperature and Density. 3. The Ground State Energy of a Relativistic Quark Gas, *Phys. Rev. D* **16**, 1169 (1977).
- [39] A. Vuorinen, The Pressure of QCD at finite temperatures and chemical potentials, *Phys. Rev. D* **68**, 054017 (2003), arXiv:hep-ph/0305183.
- [40] A. Kurkela, P. Romatschke, and A. Vuorinen, Cold Quark Matter, *Phys. Rev. D* **81**, 105021 (2010), arXiv:0912.1856 [hep-ph].
- [41] T. Gorda, A. Kurkela, P. Romatschke, S. Säppi, and A. Vuorinen, Next-to-Next-to-Next-to-Leading Order Pressure of Cold Quark Matter: Leading Logarithm, *Phys. Rev. Lett.* **121**, 202701 (2018), arXiv:1807.04120 [hep-ph].
- [42] T. Gorda, A. Kurkela, R. Paatelainen, S. Säppi, and A. Vuorinen, Cold quark matter at N³LO: Soft contributions, *Phys. Rev. D* **104**, 074015 (2021), arXiv:2103.07427 [hep-ph].
- [43] T. Gorda, A. Kurkela, R. Paatelainen, S. Säppi, and A. Vuorinen, Soft Interactions in Cold Quark Matter, *Phys. Rev. Lett.* **127**, 162003 (2021), arXiv:2103.05658 [hep-ph].
- [44] T. Gorda, R. Paatelainen, S. Säppi, and K. Seppänen, Equation of State of Cold Quark Matter to $O(\alpha_s^3 \ln \alpha_s)$, *Phys. Rev. Lett.* **131**, 181902 (2023), arXiv:2307.08734 [hep-ph].
- [45] E. Annala, T. Gorda, A. Kurkela, and A. Vuorinen, Gravitational-wave constraints on the neutron-star-matter Equation of State, *Phys. Rev. Lett.* **120**, 172703 (2018), arXiv:1711.02644 [astro-ph.HE].
- [46] O. Komoltsev and A. Kurkela, How Perturbative QCD Constrains the Equation of State at Neutron-Star Densities, *Phys. Rev. Lett.* **128**, 202701 (2022), arXiv:2111.05350 [nucl-th].
- [47] T. Gorda, O. Komoltsev, and A. Kurkela, Ab-initio QCD Calculations Impact the Inference of the Neutron-star-matter Equation of State, *Astrophys. J.* **950**, 107 (2023), arXiv:2204.11877 [nucl-th].
- [48] R. Somasundaram, I. Tews, and J. Margueron, Perturbative QCD and the neutron star equation of state, *Phys. Rev. C* **107**, L052801 (2023), arXiv:2204.14039 [nucl-th].
- [49] D. Zhou, What does perturbative QCD really have to say about neutron stars, (2023), arXiv:2307.11125 [astro-ph.HE].
- [50] C. E. Rhoades, Jr. and R. Ruffini, Maximum mass of a neutron star, *Phys. Rev. Lett.* **32**, 324 (1974).
- [51] S. Koranda, N. Stergioulas, and J. L. Friedman, Upper limit set by causality on the rotation and mass of uniformly rotating relativistic stars, *Astrophys. J.* **488**, 799 (1997), arXiv:astro-ph/9608179.
- [52] J. M. Lattimer and M. Prakash, Neutron star structure and the equation of state, *Astrophys. J.* **550**, 426 (2001), arXiv:astro-ph/0002232.
- [53] C. Drischler, K. Hebeler, and A. Schwenk, Chiral interactions up to next-to-next-to-next-to-leading order and nuclear saturation, *Phys. Rev. Lett.* **122**, 042501 (2019), arXiv:1710.08220 [nucl-th].
- [54] C. Drischler, J. A. Melendez, R. J. Furnstahl, and D. R. Phillips, Quantifying uncertainties and correlations in the nuclear-matter equation of state, *Phys. Rev. C* **102**, 054315 (2020), arXiv:2004.07805 [nucl-th].
- [55] M. M. Forbes, S. Bose, S. Reddy, D. Zhou, A. Mukherjee, and S. De, Constraining the neutron-matter equation of state with gravitational waves, *Phys. Rev. D* **100**, 083010 (2019), arXiv:1904.04233 [astro-ph.HE].
- [56] A. Cherman, T. D. Cohen, and A. Nellore, A Bound on the speed of sound from holography, *Phys. Rev. D* **80**, 066003 (2009), arXiv:0905.0903 [hep-th].
- [57] P. M. Hohler and M. A. Stephanov, Holography and the speed of sound at high temperatures, *Phys. Rev. D* **80**, 066002 (2009), arXiv:0905.0900 [hep-th].
- [58] Y. Fujimoto, K. Fukushima, L. D. McLerran, and M. Praszalowicz, Trace Anomaly as Signature of Conformality in Neutron Stars, *Phys. Rev. Lett.* **129**, 252702

- (2022), arXiv:2207.06753 [nucl-th].
- [59] A. Kurkela, K. Rajagopal, and R. Steinhorst, Astrophysical Equation-of-State Constraints on the Color-Superconducting Gap, (2024), arXiv:2401.16253 [astro-ph.HE].
- [60] M. G. Alford, K. Rajagopal, and F. Wilczek, QCD at finite baryon density: Nucleon droplets and color superconductivity, Phys. Lett. B **422**, 247 (1998), arXiv:hep-ph/9711395.
- [61] J. Berges and K. Rajagopal, Color superconductivity and chiral symmetry restoration at nonzero baryon density and temperature, Nucl. Phys. B **538**, 215 (1999), arXiv:hep-ph/9804233.
- [62] G. W. Carter and D. Diakonov, Light quarks in the instanton vacuum at finite baryon density, Phys. Rev. D **60**, 016004 (1999), arXiv:hep-ph/9812445.
- [63] R. D. Pisarski and D. H. Rischke, Gaps and critical temperature for color superconductivity, Phys. Rev. D **61**, 051501 (2000), arXiv:nucl-th/9907041.
- [64] D. T. Son, Superconductivity by long range color magnetic interaction in high density quark matter, Phys. Rev. D **59**, 094019 (1999), arXiv:hep-ph/9812287.
- [65] M. G. Alford, K. Rajagopal, and F. Wilczek, Color flavor locking and chiral symmetry breaking in high density QCD, Nucl. Phys. B **537**, 443 (1999), arXiv:hep-ph/9804403.
- [66] T. Schäfer and F. Wilczek, Superconductivity from perturbative one gluon exchange in high density quark matter, Phys. Rev. D **60**, 114033 (1999), arXiv:hep-ph/9906512.
- [67] K. Rajagopal and F. Wilczek, The Condensed matter physics of QCD, in *At the frontier of particle physics. Handbook of QCD. Vol. 1-3*, edited by M. Shifman and B. Ioffe (2000) pp. 2061–2151, arXiv:hep-ph/0011333.
- [68] M. G. Alford, A. Schmitt, K. Rajagopal, and T. Schäfer, Color superconductivity in dense quark matter, Rev. Mod. Phys. **80**, 1455 (2008), arXiv:0709.4635 [hep-ph].